Journal of
Synchrotron
Radiation

ISSN 0909-0495

Received 10 February 2010
Accepted 11 June 2010

The role of single element errors in planar parabolic compound refractive lenses

Andrzej Andrejczuk,[a]* Jacek Krzywiński,[b] Yoshiharu Sakurai[c] and Masayoshi Itou[c]

[a]Faculty of Physics, University of Bialystok, Lipowa 41, 15-424 Bialystok, Poland, [b]SLAC National Accelerator Laboratory, 2575 Sand Hill Road, Menlo Park, CA 94025, USA, and [c]Japan Synchrotron Radiation Research Institute (JASRI), SPring-8, 1-1-1 Kouto, Sayo-cho, Sayo-gun, Hyogo 679-5198, Japan. E-mail: andra@alpha.uwb.edu.pl

The propagation of X-rays through a compound refractive lens (CRL) with imperfect CRL elements is investigated. The trajectories of random rays within the geometrical optics regime are calculated in one plane using Monte Carlo methods. Three different lenses were simulated: Be, Al and Ni lenses designed for photon energies of 20 keV, 60 keV and 175 keV, respectively. The results show that while transverse displacements of single elements in a CRL do not influence imaging resolution, rotational errors can be important. Systematic calculations of aberrations owing to the deviation of the element's surface from a perfect parabolic shape are also presented.

Keywords: compound refractive lens; X-ray optics; errors in the lens; ray-tracing.

1. Introduction

X-ray refractive optics have became a powerful tool for scattering experiments, as well as for X-ray imaging. In the X-ray regime the difference between the refractive index of materials and unity is very small. Therefore, to obtain a reasonably short focusing length, X-ray refractive lenses are made from stacks of many single elements. The main drawback of X-ray refractive lenses is their small effective aperture caused by photon absorption in the material of the lenses. However, owing to the high brightness of present and future synchrotron sources, one can use such lenses quite efficiently. Moreover, the absorption can be reduced using kinoform methods (Nazmov *et al.*, 2005).

A detailed description of the properties of compound refractive lenses (CRLs) can be found by Lengeler *et al.* (2005) and Schroer *et al.* (2001). Recently, Snigirev & Snigireva (2008) have presented a review of high-energy X-ray micro-optics where CRLs were compared with mirrors, capillaries, waveguides and Fresnel zone plates. Other kinds of existing refractive devices, such as multi-prism lenses (or saw-tooth lenses) (Cederström *et al.*, 2002) or prism arrays (Jark *et al.* (2004), can also be applied to concentrate X-ray beams.

Lithographic methods are the most popular methods for single-lens or lens-array fabrication (*e.g.* Nazmov *et al.*, 2007; Artemiev *et al.*, 2005; Nöhammer *et al.*, 2003; Aristov *et al.*, 2000). However, two other techniques, the pressing technique (*e.g.* Lengeler *et al.*, 2001; Andrejczuk *et al.*, 2007) and producing bubbles in a micro-capillary (*e.g.* Huang *et al.*, 2009; Dudchik *et al.*, 2003), have been applied. Lithographic methods can be very accurate not only in obtaining the shape of the surface of the lenses but also in aligning them together. Other techniques seem less accurate. However, in some cases the highest precision is not required to obtain a good lens performance (Snigirev & Snigireva, 2008).

Several authors have used ray-tracing methods to simulate CRLs and to investigate the influence of fabrication errors on their performance (Elleaume, 1998; Protopopov, 1999; Dudchik *et al.*, 2000; Evans-Lutterodt *et al.*, 2003; Alianelli *et al.*, 2007; Umbach *et al.*, 2008). The problem of the misalignment of single lenses with respect to the optical axis of the CRL has already been discussed (Elleaume, 1998; Protopopov, 1999; Pantel *et al.*, 2001*a*,*b*; Piestrup *et al.*, 2001). Protopopov (1999) also discussed the effect of bending the whole stack of compound lenses. In this work we used our own ray-tracing program to test the systematic misalignment of conical surface axes of single elements in the stack, and also calculated the focus broadening connected with the departure of single lens surfaces from parabolic shape. The set-up for magnetic Compton scattering experiments at the BL08W beamline at SPring-8 was taken as an example for modelling the geometry in our simulations. Our calculations have been designed to test the geometry used in experiments with a planar Ni refractive lens at 175 keV (Andrejczuk *et al.*, 2006, 2007). Therefore, we developed a ray-tracing program which calculates the trajectories of rays in one plane (two dimensions). A brief description of the method was given by Andrejczuk *et al.* (2006). While we have concentrated on the performance of a Ni lens for 175 keV photon energy, we have also simulated the focusing performance of an aluminium lens for 60 keV and a beryllium lens for 20 keV photon energy.

The CRL was located 47 m from the source and was designed to image the source at 3.5 m. We assume an incoherent source chosen in such a way that the geometrical image

size is slightly below the diffraction limit determined by the CRL's effective aperture.

In Compton scattering experiments it is important to have not only an intense beam in the focus but also to minimize the surrounding background. Therefore, using various approximations, we estimated the background caused by Rayleigh and Compton scattering occurring in the lens material.

In the following section we describe the method of the calculations. We then present results of simulations for different types of errors in the lenses, followed by a discussion and summary.

2. Calculations

We consider the focusing of an X-ray beam in one plane only (planar lens). The vectorized Monte Carlo procedure (*e.g.* Bobrowicz *et al.*, 1984) for ray-tracing in two dimensions within geometrical optics laws has been written in *Matlab*. The lens shape is described by a general conical curve of eccentricity e and radius of curvature p at the vertex (Fig. 1). The eccentricity defines the type of conical curve: one obtains a circle when $e = 0$, an ellipse when $0 < e < 1$, a parabola for $e = 1$, and a hyperbola for $e > 1$. N single biconcave lenses of thickness l are situated in the external coordination system XY shown in Fig. 2. Parameters e and p, as well as the position of the vertex and the angle between the axis of the conic and the X axis, were varied during the simulations. We assumed perfectly smooth surfaces. We also assumed homogeneous lens material. Small-angle scattering from surface and bulk inhomogeneities (Elleaume, 1998; Lengeler *et al.*, 1998) was not considered here.

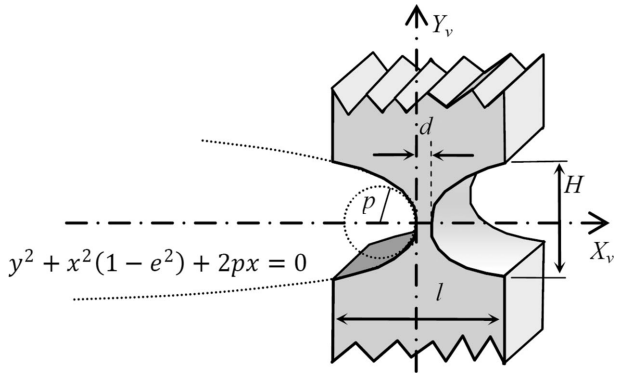

Figure 1
Layout of a single lens. The lens is a plate of thickness l where on both sides parabolic-like grooves are defined. The shape of the grooves is described by a general conical curve with equations in the coordination system centred at its vertex (X_vY_v), as shown in the figure. The curve is parameterized by the radius of curvature at vertex p and eccentricity e. The physical aperture of the lens H, and the thickness between vertexes d, are also shown.

The program simulates a set of rays (photons) that is emitted from the source, then transmitted by the lens and, finally, detected at the screen. The single ray is defined by its origin (x, y) and the r_y projection of its unit vector. The rays are randomly generated in the source volume within a range of parameters such that the height of the primary beam at the entrance of the lens is smaller than 2 mm. The intersection points of the rays with conical curves and lines are calculated on the basis of an analytical solution. When the intersection of a ray with a conical curve (or a flat part of the lens) occurs, the new direction r_y' is derived using the refraction law. The ray is propagated to the next optical element. After each intersection new parameters describing the downstream ray are calculated. Finally, if the ray has not been absorbed, the intersection F_y (Fig. 2) of the refracted ray with the screen is calculated. The histogram of the y coordinates of the intersection points F_y gives the intensity distribution at the sample surface. The histogram of the x coordinate of F_x (Fig. 2) is also calculated. In the case when the image is formed on the optical axis the mean value gives the image position and the standard deviation of F_x describes its depth.

For every ray its own photon energy parameter is assigned. The index of refraction of the lens material associated with a given photon energy is calculated using the approach presented by Lengeler *et al.* (1998). In the calculations presented here the sources were strictly monochromatic. We use different energies when we simulate the background owing to Rayleigh and Compton scattering.

The source was situated at a distance of −47 m (x_u; Fig. 2) and the screen was situated at a distance of 3.5 m (x_s; Fig. 2). The source was modelled as a Gaussian spot with a second spatial moment $\sigma = 0.6$ µm in the y direction and 1 µm in the x direction. The resulting spot size on the screen was of the

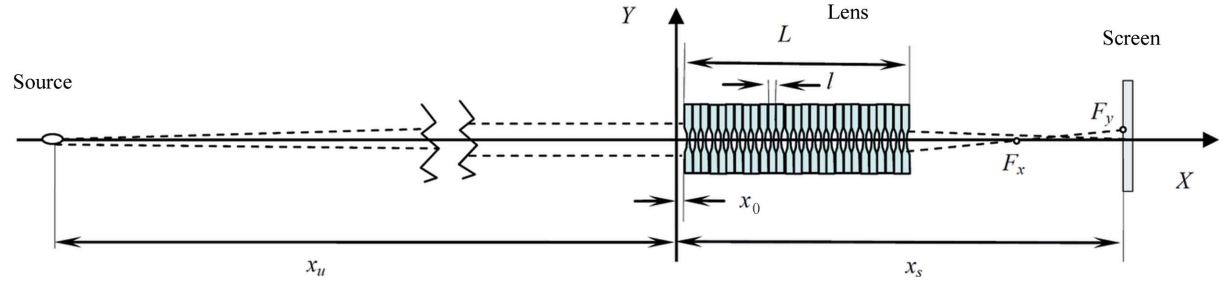

Figure 2
The geometry used in the simulations. The coordination system XY is plotted using solid thick lines. The broken lines mark the propagated beam. The X coordinates of the source, front of the lens and the screen are $-x_u$, x_0 and x_s, respectively. l and L are the thickness of a single lens and the total length of the compound lens, respectively. F_x and F_y are the intersection points of the refracted ray with the X axis and the screen plane, respectively. The proportions of the objects in the figure do not correspond to the real situation.

Table 1
Parameters of simulated lenses.

The type of lens material and the energy of radiation are shown in the first row. The following rows contain values of the parameters corresponding to the three different lenses: p is the radius of curvature at the vertex, N is the number of biconcave lenses, μ is the linear attenuation coefficient, δ is the refraction index decrement ($n = 1 - \delta$), x_0 is the position of the front of the CRL in the X direction (Fig. 2), l is the thickness of the single biconcave lens, L is the total length of the CRL and H is the geometrical aperture of the lens.

	Be 20 keV	Al 60 keV	Ni 175 keV
p (μm)	200	150	100
N	37	157	274
μ (cm^{-1})	0.3957	0.7507	1.615
$\delta \times 10^{-7}$	8.520	1.500	0.5761
x_0 (mm)	47.13	−24.90	9.16
l (mm)	2.00	1.00	0.50
L (cm)	7.4	15.7	13.7
H (μm)	1264	773.9	445.6

order of 0.1 μm. This is comparable with the diffraction limit for the model geometry. We adjusted the front lens position (x_0 in Table 1, Fig. 2) to obtain the source image exactly at the fixed screen location.

Although different numbers of rays were used in particular simulations, the intensity I_0 of the source beam was normalized to the value 10^6 photons m^{-1} measured at the screen position, with no lens in the way. The calculated intensity distribution dN/dy at the screen represents the ratio of the number of detected photons dN in the interval dy. The intensity distribution dN/dy is expressed in units of counts m^{-1}. CRL errors both change the shape of the beam and can shift its vertical position. The range of the histogram was adjusted to secure a proper description of the beam profile at the screen.

To be sure that our numerical method was accurate enough, we compared the results of simulations of a parallel beam passing a single lens with the results derived from an analytical solution. We found that the accuracy of the simulation of the vertical intensity distribution was of the order of 10^{-10} m.

Three different lenses were taken into consideration: a beryllium lens for 20 keV, an aluminium lens for 60 keV, and a nickel lens for 175 keV photon energy. The parameters of all three lenses are shown in Table 1. For all cases the eccentricity e was equal to $1 - \delta$ (Evans-Lutterodt *et al.*, 2003), except when the relation between the broadening of the image and the eccentricity was investigated. The thickness between vertices was 3 μm, the smallest value for which rotated parabolas did not intersect. All CRLs (if perfectly aligned) gave a sharp image of the source at 3.5 m. The image had a Gaussian profile with a full width at half-maximum (FWHM) of 0.1 μm. The intensity of the image was different for each CRL owing to the different level of absorption (Fig. 3). The model beam size (2 mm) at the entrance of the lens is substantially wider than the physical aperture in order to accept changes in the position of the lens owing to introduced errors. The direct transmission by the flat part of the Be, Al and Ni CRLs was 5.0×10^{-2}, 7.6×10^{-6} and 2.4×10^{-10}, respectively. We characterize the size of an image on the screen by a width parameter W. This is obtained by calculation of the second

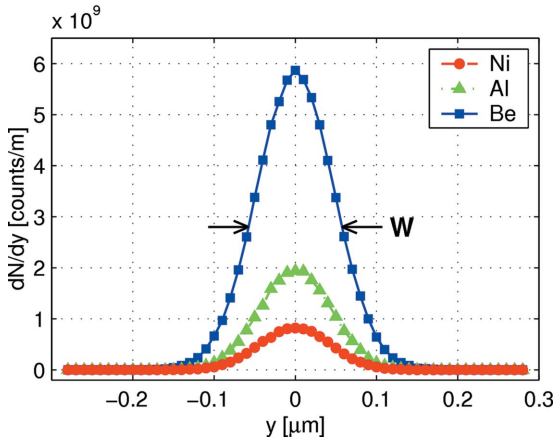

Figure 3
The simulated beam profile at the screen position for perfectly aligned Be, Al and Ni lenses. The histograms were obtained with the emission of 1.2×10^6 rays for each lens. All beams have width W roughly equal to 0.1 μm.

moment (RMS) of a simulated distribution and multiplying it by 2.35. The mean value of the intensity distribution gives the vertical position of the beam which we call hereafter the centre of the beam (C).

Absorption in the lens material was modelled by the random removal of rays during propagation. The probability of this process was calculated on the basis of available cross-section data (McMaester *et al.*, 1969) (photoelectric absorption, Rayleigh and Compton scattering) and the path length inside the single lens. The correctness of this method has been checked in separate simulations with a set of flat model absorbers. The detected intensity was in full agreement with the values calculated from the $I_0 \exp(-\mu t)$ dependence. We also simulated the transmission profile by a single concave parabolic lens and good agreement with analytical predictions was found. Rays that were supposed to be totally reflected were removed from the beam. However, such cases were very rare and did not influence the results.

We estimated the background due to Rayleigh and Compton scattering by additional simulations of scattering in three dimensions and performing a projection back to two dimensions (Andrejczuk *et al.*, 2006). This was done with additional constrains. The rays which scattered by more than 60° were removed from the set and accounted for as absorbed rays. Only one scattering per single ray was allowed during a single lens passage. If the energy of the scattered ray changed, the refraction was calculated for the new energy. The simulations showed that the intensity distribution of the scattered background was flat in the region of a few millimetres around the focus. Its intensity was roughly proportional to the total intensity transmitted by the lens. This suggests that the background was generated in the part of the lens which was close to the CRL exit. The level of the background was quite small (Table 2, first row). Taking into account that the projection into two dimensions overestimates the real effect, the contribution of the scattering to the total intensity distribution can be neglected. Therefore we show most of our results without accounting for the scattering.

Table 2
Parameters obtained from simulations.

The type of lens material and the energy of radiation are shown in the first row. I_{bckg} is the intensity of the Rayleigh–Compton background. I_{int} is the integral of dN/dy for the ideal case. A_{eff} and $A_{eff}^{(1)}$ are effective apertures resulting from simulations and from equation (1), respectively. A_{eff}/p is the ratio of the effective aperture of a CRL lens and the radius of curvature of a single lens. dC/dα_b is the coefficient of the vertical shift of the centre of the beam owing to the bending error.

	Be 20 keV	Al 60 keV	Ni 175 keV
I_{bckg} (counts m^{-1})	34 (4)	16 (3)	7.3 (4)
I_{int} (counts)	694 (2)	216.3 (6)	90.5 (4)
A_{eff} (μm)	694 (2)	216.3 (6)	90.5 (4)
$A_{eff}^{(1)}$ (μm)	655	200	84.3
A_{eff}/p	3.48	1.44	0.905
dC/dα_b (μm mrad^{-1})	0.67	0.22	0.12

3. Results

Fig. 3 shows the results of simulations of the beam profile when all elements were perfectly aligned, the eccentricity $e = 1 - \delta$, and 1.2×10^6 rays were emitted from the source into a 2 mm aperture in front of the lens. The number of rays which reached the screen was 4.12×10^5, 1.21×10^5 and 0.50×10^5 for the Be, Al and Ni lenses, respectively. These numbers represent typical values, which were used to calculate histograms and resulting parameters. The integral of the distribution gives us the integral intensity I_{int} detected on the screen (Table 2). The accuracy of the calculated parameters is roughly 1%, and the statistical uncertainty of W parameters is smaller than the size of the points in the figures.

The effective aperture A_{eff} is often discussed in the literature. Different definitions can be found, but the one used most frequently is the aperture A_{eff} which transmits the same number of rays as the lens does. For a parabolic planar lens, assuming parallel rays propagating through the lens and $d = 0$, this approach gives a simple expression (see, for example, Jark *et al.*, 2004),

$$A_{eff}^{(1)} = (2\pi)^{1/2} [\, p/(\mu 2N)]^{1/2}, \qquad (1)$$

where μ is the linear attenuation coefficient and N is the number of double concave lenses. Because the normalization of the direct beam is 1 photon μm^{-1}, I_{int} also gives the simulated effective aperture A_{eff} expressed in micrometres (Table 2). Results of simulations fit quite well with expression (1) [$A_{eff}^{(1)}$, Table 2]. A_{eff} has slightly higher values than $A_{eff}^{(1)}$ despite $d \neq 0$. This is connected to the fact that the rays go through the CRL in bent trajectories and more rays pass the thinner part of the lenses than in the configuration used to derive $A_{eff}^{(1)}$. For a lens with parabolic shape the transmission profile is a Gaussian, with its FWHM equalling roughly A_{eff}.

We investigated the rotations of the entire planar CRL around the axis perpendicular to the XY plane (the axis of grooves direction) and passing through the centre of the lens. We found that the intensity drops by 10% for rotations of 4.20, 0.78 and 0.40 mrad for the Be, Al and Ni lenses, respectively. These numbers are approximately half of the value of the angles corresponding to the ratio of the effective aperture A_{eff} and the total length of the lens L. No visible change of the width W of the focused beam has been observed within this range of angles. The parabolic and the sinusoidal deformation of the entire CRL in the Y direction as a function of the amplitude of the deformation have also been investigated. No broadening of the beam was found before the beam's intensity dropped substantially.

3.1. Misalignment of parabola axis: rotation

As seen above, rotations of the entire CRL cannot be large if one wants to preserve the transmission. However, all parabola axes can be systematically rotated by an angle α_r. This can happen when a fabrication pressing device is misaligned in such a way that produces grooves shown in the inset in Fig. 4. We will call it rotation error. Simulations find that for such a systematic error the centre of the beam does not shift ($C = 0$) and the integral intensity does not change for rotations of parabola axes up to 100 mrad. For higher angles the integral intensity decreases quickly.

The dependence of the peak width W on the value α_r exhibits a threshold behaviour illustrated in Fig. 4. The broadening depends on the lens type, and the width W reaches 1 μm for a 11, 34 and 66 mrad rotation of the Be, Al and Ni lenses, respectively. The situation does not change when every second double-concave lens is rotated by 180° around the optical axis, which effectively corresponds to a change of the sign of rotations of the parabolas ($-\alpha_r$).

3.2. Misalignment of parabola axis: bending

The CRL performance worsens if we assume a deformation where the parabolas on both sides of the double concave lens are rotated in opposite directions. This can happen when the two pressing tools systematically press in slightly different directions and produce all lenses as shown in the inset of Fig. 5. Here we call this the bending error. Simulations show that if the bending error is the same in all single lenses the beam profile changes even for small bending angle α_b. Fig. 5 shows the width W of the beam profile at the screen position as a

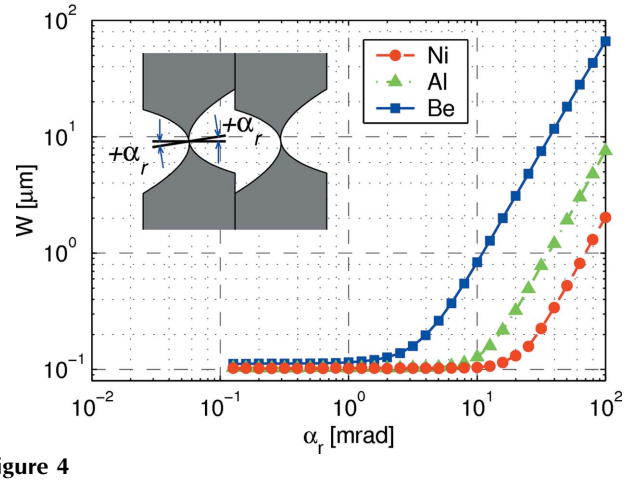

Figure 4
Dependence of the width of the beam profile on the rotation angle α_r. The inset shows parabolas rotated by 0.16 rad.

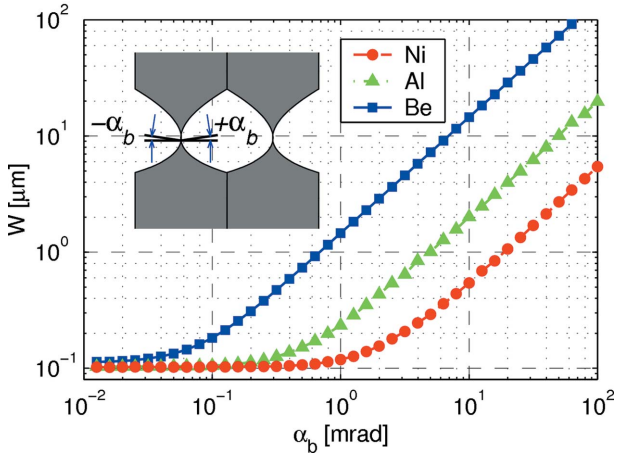

Figure 5
Dependence of the width of the beam profile on bending angle α_b. The inset shows parabola axes bent by 0.16 rad.

function of the bending angle α_b. The width W reaches a value of 1 μm for 0.7, 5 and 19 mrad bending for the Be, Al and Ni lenses, respectively.

Up to 100 mrad, rotation and bending do not reduce the integral intensity transmitted by the lens. However, bending changes the position of the beam centre C. Fig. 6 shows examples of beam shapes influenced by rotation and bending errors for the Ni CRL. As can be seen, the beam keeps its position in the presence of rotation errors (green triangles). It moves and becomes asymmetric when bending errors are introduced (red circles). Simulations show that the centre of the beam moves roughly linearly with α_b with the coefficient $dC/d\alpha_b$ shown in Table 2. The results show that among the three CRL lenses discussed the beryllium CRL is most sensitive to rotation and bending errors.

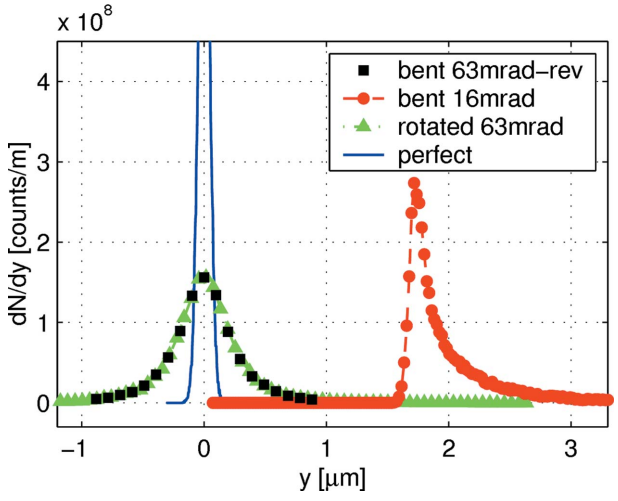

Figure 6
Examples of the beam profile for a Ni 175 keV lens for different states of parabola axes misalignment. The profile for the undisturbed lens is plotted by the blue solid line. The red circles represent bending by 16 mrad and the green triangles represent rotation by 63 mrad. The black squares show bending of 63 mrad but for a CRL having every second lens reversed (rotated by 180° around the optical axis).

The effect of bending is similar to that of rotation if one changes the bending direction of every second lens by rotating it by 180° around the optical axis. Indeed, as seen in Fig. 6, bending by 63 mrad and reversing every second lens (black squares) gives a beam profile equivalent to that obtained with rotations by the same angle (green triangles). We have also simulated the CRL with random distribution of the parabola rotation angles. The smearing of the image caused by the random rotations is similar to the systematic rotation discussed above in the case of the Al and Ni lenses. For the beryllium lens, which has a relatively small number of elements, the fluctuations do not average as well as in the case of the two other lenses. For the beryllium lens the width W reaches 1 μm for $\sigma(\alpha_r) = 2$ mrad.

3.3. Misalignment of parabola axes: transversal shift

That the resolution does not depend on a transverse shift of the parabolas has been reported many times in the literature. We also simulated vertical shifts s of the lenses. The shift is illustrated in the inset in Fig. 7. A systematic shift occurs when all lenses have the same shift error s. The dependence of the integral intensity on the shift s is shown in Fig. 7. The intensity drops by 10% for shifts s of 15.6, 36.8 and 102 μm for the Ni, Al and Be lenses, respectively. The shape of the beam and its width W and position C do not depend on the s value in the investigated range of the s parameter.

We have also simulated random fluctuations of the vertical shifts s. The dependences of integral intensity on the standard deviation $\sigma(s)$ is practically the same as those shown in Fig. 7 when s is replaced by $\sigma(s)$. As noticed by Pantell *et al.* (2001*a*), a transverse shift does not influence the image shape but reduces the CRL transmission by adding a thickness $\Delta d = \sigma^2/p$ to the effective thickness of a double concave lens. This results in the following reduction of the CRL transmission,

$$I = I_0 \exp\left[(-\mu\sigma^2 N)/p\right], \qquad (2)$$

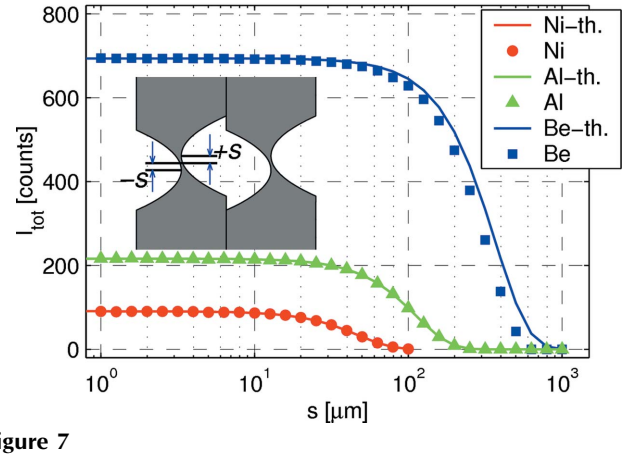

Figure 7
The integral intensity detected at the screen *versus* the transversal shift s. Points represent results of the simulations. Lines represent theoretical predictions based on equation (2) where s was inserted instead of σ, and I_0 was set to the integral intensity obtained for the perfect lens.

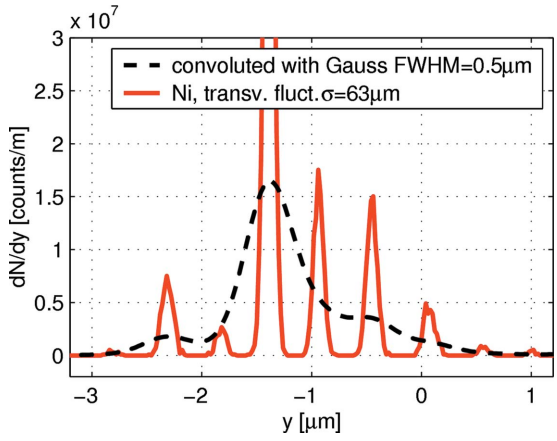

Figure 8
Example beam profile for the Ni lens with high transversal random fluctuations of $\sigma(s) = 63$ μm. The solid line represents the result of simulations. The broken line represents the profile convoluted with the Gaussian of FWHM = 0.5 μm. The maximum of the main peak is 8×10^7 counts m^{-1}.

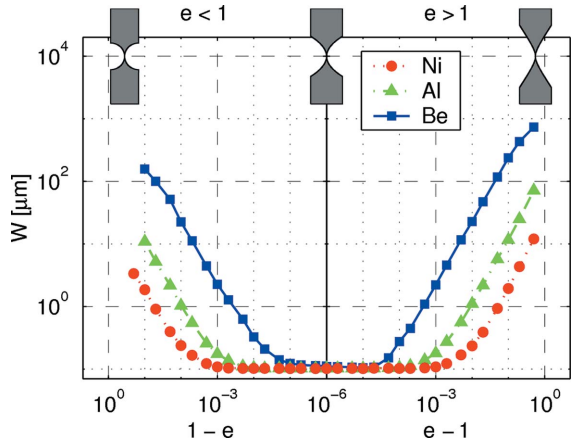

Figure 9
The width W of the beam profile at the screen *versus* the eccentricity e. The left-hand and right-hand parts show data for $e < 1$ and $e > 1$, respectively. The direction of the left-hand horizontal axis is reversed. The insets show the shape of the lenses of the same radius of curvature p = 200 μm and e = 0.3, 1 and 1.8 from left to right.

where σ is the standard deviation of the fluctuations of the transversal shift and N is the number of double concave lenses. Our numerical simulations agree very well with the results obtained from this simple expression (2) (see Fig. 7). We have also observed, as reported by Protopopov (1999), that for different fluctuations one obtains different vertical shifts of the focus. For a given realisation of the fluctuations the focus position changes linearly with σ. The width W of the peak at the screen position does not depend on σ.

For large transverse fluctuation amplitudes the flat part of the lenses can enter the region where the beam is transmitted and small satellites appear around the central peak. This can be seen in Fig. 8 which shows the beam profile simulated for the Ni lens with large fluctuations of the shift s (normal distribution). In our model case, σ = 63 μm and the integral intensity is 15 counts. The satellites appear for a certain amplitude of fluctuations and then their intensity increases with σ while the intensity of the main peak decreases. The intensity of individual satellite peaks varies strongly from one configuration to another. However, they are very regularly spaced in the y direction, and the period depends on the lens parameters. We have found that the periods are 9, 1.5 and 0.5 μm for the Be, Al and Ni lenses, respectively.

3.4. Broadening owing to departure from parabolic shape

In the literature, parabolic lenses are reputed to give the smallest aberrations for CRLs. We checked this assertion with our simulations. We made a series of simulations varying the eccentricity e while keeping other parameters constant (Table 1). Fig. 9 shows the width W of the beam profile at the screen position as a function of $(e - 1)$ plotted on a logarithmic scale. The figure is divided into two parts, where the left-hand side and right-hand side show the results for $e < 1$ and $e > 1$, respectively. The direction of the horizontal axis in the left-hand part of the figure was reversed. In the centre of the figure the lens's shapes are close to a parabola, at the left-hand boundary the lens's surfaces are circular, and at the right-hand boundary they have hyperbolic shapes as shown by the insets in Fig. 9.

An increased image width W up to 1 μm occurs when the value $|1 - e|$ approaches 0.00045, 0.0090 and 0.053 for the Be, Al and Ni lenses, respectively. It is interesting that if we calculate the change of the lens width at the place which corresponds to the effective aperture $A_{\rm eff}$ then for all lenses we obtain roughly the same value of 0.2 μm. This number can represent the required precision of the machining process when one aims at 1 μm focusing.

4. Discussion

Our simulations indicate that the performance of a CRL is most sensitive to bending errors of the individual lenses. In the case of the beryllium lens even small but systematic bending can influence the quality of imaging. The lenses are small objects and 1 mrad of rotation corresponds to a deformation of the order of 1 μm. This kind of error can easily appear when the pressing technique is used for the fabrication of the lenses. When strong bending errors are present our simulations imply that rotating every second lens by 180° around the optical axis reduces the aberrations by one order of magnitude. It was shown in §3.2 that the sensitivity to the rotation and bending angles is similar when one applies the above reversing procedure.

The dependence of the width W on $\alpha_{\rm r}$ and $\alpha_{\rm b}$ can be discussed in terms of optical aberrations. It can be shown that for small angles of rotation of the parabola the ray's path Δx inside the single concave parabolic lens, as a function of distance y from the optical axis, is equal to

$$\Delta x = \frac{y^2}{2p} - \left(y + \frac{y^3}{2p^2}\right)\alpha + \left(\frac{y^2}{2p} + \frac{5y^4}{8p^3}\right)\alpha^2. \qquad (3)$$

The first term is the path for the non-rotated parabola. The second term, which is proportional to α, contains aberrations known as the tilt and the coma. The third term, proportional to α^2, contains aberrations known as the spherical aberration and the defocus. In the case of a double concave lens with rotation error the terms with the odd powers of α are cancelled. For the bending error these terms are doubled. This qualitatively describes the character of the aberration observed in the simulations. In the case of bending errors we observe strong aberrations owing to the coma and the tilt, and the width of the beam is proportional to α_b. This is clearly illustrated in Fig. 6, where the shape of the focal spot and the shift of its position correspond to the coma and the tilt aberration, respectively. In the case of the rotation errors the spherical aberration and the defocus have a much smaller influence on the width W as they are proportional to α_r^2. One can also note that the slopes of the curves plotted on log–log scales in Figs. 4 and 5 differ by a factor of two. This reflects the fact that the effect of the rotation errors is proportional to α_r^2, and the effect of the bending errors is proportional to α_b. Equation (3) also explains why, in the case of the stack of N double concave lenses, reversing every second lens reduces the aberrations. In this case the tilt and the coma terms are again cancelled.

It seems that an accuracy of 0.01 mm is technically achievable in the pressing technology. For the elements of size 1 mm this corresponds to angles of the order of 10 mrad. As the simulations show (Fig. 4), for Ni and Al lenses this level of angular error has no influence on the lens resolution. However, in the case of the beryllium lens, the angular errors should be smaller than 2 mrad.

The sensitivity of the performance of the lens to the rotation, the bending and the changes in e is correlated with the ratio of the effective aperture and the radius of curvature ($A_{\rm eff}/p$, Table 2). Additional simulations performed for modified lenses Be (longer, N = 194, p = 1000 µm, $A_{\rm eff}/p$ = 0.70) and Ni (similar length but N = 56 and p = 20 µm, $A_{\rm eff}/p$ = 4.53) seem to confirm this statement; we obtained the smallest aberration for the Be lens and the highest aberration for the Ni lens. Qualitatively this is in accordance with the aberration terms in equation (3). When we increase the p factor the aberration terms in the optical path decrease.

The above argument might suggest that the lenses with larger radii are better because they are less sensitive to the rotational and the shape errors. However, one should keep in mind that the larger p requires a higher N number of the CRL's elements for a given focal length. In a real CRL the thickness d between parabola vertices is of the order of tens of micrometres, and with a large number of the elements the transmission is substantially reduced. This is especially the case for CRLs operating at a high photon energy. For example, the Ni lens operating at 175 keV has 274 double concave lenses. For d = 10 µm it gives 54 counts of the integral intensity in comparison with 90 for d = 0 (for the incident beam of intensity 1 photon µm^{-1}). The increase of p by a factor of two will result in doubling the number of lenses and the reduction of the integral intensity to 33 counts. On the contrary, the reduction of p by a factor of two will reduce the number of lenses by two and increase the integral intensity to 69 counts. Therefore, for focusing of high-energy X-rays, lenses with a smaller radius of curvature are desirable. Also, the reduction of p can substantially decrease the cost of the CRL if fabrication of a single element is expensive.

From a practical point of view the shift of the beam is not as important as the image broadening. Usually positioning of the beam is performed using scans of the vertical position of the lens, and the small shift can be easily cancelled. Simulated shifts of the beam owing to bending are small. For α_b = 10 mrad the shift is several micrometres. The simulations show that for a wide range of angles the shift of the centre of the beam C is linear in α_b.

The insensitivity of the focusing quality of the compound parabolic lens to transversal shifts of its elements is confirmed in our simulations. For both systematic and small random shifts we observed a single peak with constant width W. However, satellites appear for error distributions where only a few lenses are vertically displaced far enough from the optical axis that their flat parts come close to the region where the beam is still transmitted. An example of such a distribution is a normal one with the size of the standard deviation σ_a that fulfills the above condition. This leads to the equation for the threshold of the standard deviation for which the satellites can appear,

$$\sigma_a = \frac{1}{2}\left(\frac{H}{2} - A_{\rm eff}\right). \qquad (4)$$

The threshold level given by the above equation agrees with the threshold observed in simulations.

To obtain a quantitative description of the period of the satellites we consider a single parabola shifted up by a distance $s = (H/2) - A_{\rm eff}$. In this case the transmitted part of the beam reaches the flat part of the lens. The part of the beam passing through the flat part of the lens is less focused and crosses the X axis at $\Delta x = x/2N$ further than the main image. Because this happens for the rays propagating at distance $A_{\rm eff}$ below the optical axis, this part of the beam crosses the screen at $\Delta y_1 = A_{\rm eff}\Delta x/x$ below the main image. The shift s of the lens causes a small upward shift of the main image that is equal approximately to $\Delta y_2 = s/2N$. The distance Δy between the two parts of the beam will be the sum of Δy_1 and Δy_2 so we obtain the approximate expression

$$\Delta y = \frac{A_{\rm eff}}{2N} + \frac{(H/2) - A_{\rm eff}}{2N} = \frac{H}{4N}. \qquad (5)$$

It is evident from (5) that the period of satellites is proportional to the physical aperture, and is inversely proportional to the number of lenses. Equation (5), derived under the assumption that the source is at infinity, describes the observed period of satellites with an accuracy of 10%.

Owing to the large number of elements in the Ni CRL the space between satellites is small. When such a lens is used to image a large source, the satellites will produce a smeared background around the main peak. This can be seen in Fig. 8 where the simulated beam profile has been convoluted with a Gaussian profile of FWHM width equal to 0.5 µm. It is note-

worthy that for lenses such as the beryllium lens, discussed in this paper, the transmission is non-zero for the entire physical aperture. Therefore, the satellites appear even for a very small amplitude of fluctuations. One can avoid the appearance of the satellites by using an additional diaphragm with a sufficiently small aperture in the front of the CRL.

A broad background can appear owing to Rayleigh and Compton scattering in the lens material. However, its level is low. Let us consider an example where the sample's size is of the order of 3 μm, and is placed on a substrate of size 1 mm. In this case the scattering in the CRL material will give an integral background $\sim 10^{-4}$ smaller than the integral signal from the sample in a Compton scattering experiment.

It should be stressed that the results presented here are valid for planar lenses only. The rotational errors, which strongly influence the focus quality, can be less important in two-dimensional focusing when the random fluctuation of the paraboloid axes are distributed in space, and not in the plane, as in our calculations.

5. Summary

The ray-tracing program for simulations of the performance of planar compound refractive X-ray lenses has been described. We have investigated the influence of misalignment of symmetry axes of surfaces of CRL elements on the focusing performance. Two types of misalignment errors were considered: rotation errors when two collinear axes of conical surfaces of a biconcave lens were rotated with respect to the CRL axis, and bending errors when two axes were bent with respect to each other. Calculations made for three different CRLs showed that these errors can be important for lenses with a high ratio of effective aperture to radius of curvature at the vertexes. In particular, systematic bending errors can cause aberrations which make the beam broader, asymmetric and shifted. However, the influence of the bending errors can be reduced to the rotation errors, which give smaller aberrations, by reversing every second biconcave lens. The analysis also showed that the deviation from parabolic shape has to be smaller than a fraction of a micrometre at the radius of the effective aperture if one wants to achieve focusing of better than 1 μm on a distance of a few metres. The simulation confirmed that a small transversal displacement of the individual lenses has no influence on the quality of focusing. However, it was found that, for a large amplitude of the random fluctuations, satellites with constant period can appear around the main focus.

References

Alianelli, L., Sánchez del Río, M. & Sawhney, K. J. S. (2007). *Spectrochim. Acta B*, **62**, 593–597.

Andrejczuk, A., Sakurai, Y. & Itou, M. (2006). *IPAP Conf. Ser.* **7**, 162–164.

Andrejczuk, A., Sakurai, Y. & Itou, M. (2007). *AIP Conf. Proc.* **879**, 994–997.

Aristov, V. V., Grigoriev, M., Kuznetsov, S. M., Shabelnikov, L. G., Yunkin, V. A., Hoffmann, M. & Voges, E. (2000). *Opt. Commun.* **177**, 33–38.

Artemiev, A. N., Snigirev, A. A., Kohn, V., Snigireva, I., Artemiev, N., Grigoriev, M., Peredkov, S., Glikin, L., Levtonov, M., Kvardakov, V., Zabelin, A. & Maevskiy, A. (2005). *Nucl. Instrum. Methods. Phys. Res. A*, **543**, 322–325.

Bobrowicz, F. W., Lynch, J. E., Fisher, K. J. & Tabor, J. E. (1984). *Parallel Comput.* **1**, 295–305.

Cederström, B., Lundqvist, M. & Ribbing, C. (2002). *Appl. Phys. Lett.* **81**, 1399–1401.

Dudchik, Y. I., Kolchevsky, N. N., Komarov, F. F., Kohmura, Y., Awaji, M., Suzuki, Y. & Ishikava, T. (2000). *Nucl. Instrum. Methods. Phys. Res. A*, **454**, 512–519.

Dudchik, Y. I., Kolchevsky, N. N., Komarov, F. F., Piestrup, M. A., Cremer, J. T., Gary, C. K. & Pantell, R. H. (2003). *Proc. SPIE*, **5194**, 56–61.

Elleaume, P. (1998). *Nucl. Instrum. Methods. Phys. Res. A*, **412**, 483–506.

Evans-Lutterodt, K., Ablett, J. M., Stein, A., Kao, Chi-Chang, Tennant, D. M., Klemens, F., Taylor, A., Jacobsen, C., Gammel, P. L., Huggins, H., Ustin, S., Bogart, G. & Ocola, L. (2003). *Opt. Express*, **11**, 919–926.

Huang, C., Mu, B., Wang, Z., Chen, L. & Dudchik, Y. I. (2009). *Nucl. Instrum. Methods. Phys. Res. A*, **602**, 446–449.

Jark, W., Pérennès, F., Matteucci, M., Mancini, L., Montanari, F., Rigon, L., Tromba, G., Somogyi, A., Tucoulou, R. & Bohic, S. (2004). *J. Synchrotron Rad.* **11**, 248–253.

Lengeler, B., Schroer, C. G., Benner, B., Guenzler, T. F., Kuhlmann, M., Tümmler, J., Simionovici, A. S., Drakopoulos, M., Snigirev, A. A. & Snigireva, I. (2001). *Nucl. Instrum. Methods. Phys. Res. A*, **467–468**, 944–950.

Lengeler, B., Schroer, C. G., Kuhlmann, M., Benner, B., Guenzler, T. F., Kurapova, O., Zontone, F., Snigirev, A. A. & Snigireva, I. (2005). *J. Phys. D*, **38**, A218–A222.

Lengeler, B., Tümmler, J., Snigirev, A. A., Snigireva, I. & Raven, C. (1998). *J. Appl. Phys.* **84**, 5855–5861.

McMaester, W. H., Kerr Del Gande, N., Mallett, J. H. & Hubbell, J. H. (1969). *Compilation of X-ray Cross Sections*, UCRL-50174, Lawrence Radiation Laboratory, University of California, USA.

Nazmov, V., Reznikova, E., Snigirev, A. A., Snigireva, I., DiMichiel, M., Grigoriev, M., Mohr, J., Matthis, B. & Saile, V. (2005). *Microsyst. Technol.* **11**, 292–297.

Nazmov, V., Reznikova, E., Somogyi, A., Last, A., Mohr, J., Saile, V., Simon, R. & DiMichiel, M. (2007). *AIP Conf. Proc.* **879**, 770–773.

Nöhammer, B., David, C., Rothuizen, H., Hoszowska, J. & Simionovici, A. S. (2003). *Microelectron. Eng.* **67–68**, 453–460.

Pantell, R. H., Feinstein, J., Beguiristain, H. R., Piestrup, M. A., Gary, C. K. & Cremer, J. T. (2001*a*). *Rev. Sci. Instrum.* **72**, 48–52.

Pantell, R. H., Feinstein, J., Beguiristain, H. R., Piestrup, M. A., Gary, C. K. & Cremer, J. T. (2001*b*). *Appl. Opt.* **40**, 5100–5105.

Piestrup, M. A., Pantell, R. H. & Cremer, J. T. (2001). US Patent 6269145 B1.

Protopopov, V. V. (1999). *Opt. Commun.* **172**, 113–124.

Schroer, C. G., Tümmler, J., Lengeler, B., Drakopoulos, M., Snigirev, A. A. & Snigireva, I. (2001). *Proc. SPIE*, **4143**, 60.

Snigirev, A. A. & Snigireva, I. (2008). *C. R. Phys.* **9**, 507–516.

Umbach, M., Nazmov, V., Simon, M., Last, A. & Saile, V. (2008). *Proc. SPIE*, **7077**, 70770G.